

The Magellan/PFS Exoplanet Search: a 55-d period dense Neptune transiting the bright ($V = 8.6$) star HD 95338

Matías R. Díaz ¹★ James S. Jenkins ¹★ Fabo Feng ²★ R. Paul Butler,² Mikko Tuomi,³ Stephen A. Shtetman,⁴ Daniel Thorngren,^{5,6} Maritza G. Soto,⁷ José I. Vines ¹, Johanna K. Teske,⁴† Diana Dragomir,⁸ Steven Villanueva,⁹ Stephen R. Kane,¹⁰ Zaira M. Berdiñas,¹ Jeffrey D. Crane,⁴ Sharon X. Wang^{2,4} and Pamela Arriagada²

¹Departamento de Astronomía, Universidad de Chile, Camino El Observatorio 1515, Las Condes, Santiago, Chile

²Earth and Planets Laboratory, Carnegie Institution for Science, 5124 Broad Branch Road, Washington, DC 20015-1305, USA

³Center for Astrophysics Research, School of Physics, Astronomy and Mathematics, University of Hertfordshire, College Lane, Hatfield AL109AB, UK

⁴The Observatories, Carnegie Institution for Science, 813 Santa Barbara Street, Pasadena, CA 91101, USA

⁵Department of Physics, University of California, Santa Cruz, CA 95064, USA

⁶Institut de Recherche sur les Exoplanètes, Université de Montréal, Montréal, QC H3C 3J7, Canada

⁷School of Physics and Astronomy, Queen Mary University of London, GO Jones Building, 327 Mile End Road, London E1 4NS, UK

⁸Department of Physics and Astronomy, University of New Mexico, 1919 Lomas Blvd NE, Albuquerque, NM 87131, USA

⁹MIT Kavli Institute for Astrophysics & Space Research, 77 Massachusetts Ave. Building 37-582 BB, Cambridge, MA 02139, USA

¹⁰Department of Earth and Planetary Sciences, University of California Riverside, 900 University Ave., Riverside, CA 92521, USA

Accepted 2020 June 7. Received 2020 May 8; in original form 2020 March 23

ABSTRACT

We report the detection of a transiting, dense Neptune planet candidate orbiting the bright ($V = 8.6$) K0.5V star HD 95338. Detection of the 55-d periodic signal comes from the analysis of precision radial velocities from the Planet Finder Spectrograph on the Magellan II Telescope. Follow-up observations with HARPS also confirm the presence of the periodic signal in the combined data. HD 95338 was also observed by the *Transiting Exoplanet Survey Satellite* (TESS) where we identify a clear single transit in the photometry. A Markov chain Monte Carlo period search on the velocities allows strong constraints on the expected transit time, matching well the epoch calculated from TESS data, confirming both signals describe the same companion. A joint fit model yields an absolute mass of $42.44^{+2.22}_{-2.08} M_{\oplus}$ and a radius of $3.89^{+0.19}_{-0.20} R_{\oplus}$, which translates into a density of $3.98^{+0.62}_{-0.64} \text{ g cm}^{-3}$ for the planet. Given the planet mass and radius, structure models suggest it is composed of a mixture of ammonia, water, and methane. HD 95338 b is one of the most dense Neptune planets yet detected, indicating a heavy element enrichment of ~ 90 per cent ($\sim 38 M_{\oplus}$). This system presents a unique opportunity for future follow-up observations that can further constrain structure models of cool gas giant planets.

Key words: techniques: photometric – techniques: radial velocities – planets and satellites: detection – planets and satellites: fundamental parameters – planetary systems.

1 INTRODUCTION

As the transit probability of a planet orbiting a star decreases with increasing orbital period, or star–planet separation, the majority of transiting systems contain planets with orbital periods of less than 10 d. For planets with longer periods, not only does the probability decrease compared with the shorter period counterparts, but they are also much more difficult to detect and confirm logistically, using ground-based transit surveys. Large-scale surveys have been set up to try to target longer period transiting systems (e.g. HATSouth, Bakos et al. 2013; NGTS, Wheatley et al. 2017), but they are generally limited to detection sensitivities that fall off after 12 d, due to the observing window function problem (Bakos et al. 2013). Space-based

surveys can bypass this issue, as they are capable of monitoring these targets almost continuously.

The *CoRoT* (Baglin et al. 2006), *Kepler* (Borucki et al. 2010), and *K2* (Howell et al. 2014) space missions paved the way for the *Transiting Exoplanet Survey Satellite* (TESS; Ricker et al. 2015) mission. *CoRoT* and *Kepler*, in particular, were able to provide some startling discoveries, particularly giving a first glimpse into the structural properties of small planets (e.g. *CoRoT*-7b, Léger et al. 2009; *Kepler*-10 b, Batalha et al. 2011). However, what we have learned about giant planets has mainly come from ground-based planet detections, due in no small part to the ease of radial velocity (RV) follow-up, which is a requirement to constrain the mass and density of transit detections.

Detailed studies have been possible for a handful of gas giant planets. For example, two of the most well-known planets are HD 189733 b (Bouchy et al. 2005) and HD 209458 b (Henry et al. 2000). HD 209458 b was the first confirmed transiting planet (Charbonneau

* E-mail: matias.diaz.m@ug.uchile.cl (MRD); jjenkins@das.uchile.cl (JSJ); ffeng@carnegiescience.edu (FF)

† NASA Hubble Fellow.

et al. 2000) and was also the first that allowed us to detect elements in its escaping atmosphere, in this case, Na and CO (Charbonneau et al. 2002). HD 189733 b also orbits a fairly bright star, and therefore we also found this object to have an inflated atmosphere that is in the process of being evaporated due to the close proximity of the host star (Lecavelier des Etangs et al. 2012; Bourrier et al. 2013). From its escaping atmosphere, sodium D absorption has been characterized (Wytttenbach et al. 2015; Salz et al. 2016). Recent studies have revealed water vapour absorption on the planet’s atmosphere (Birkby et al. 2013; Alonso-Floriano et al. 2019) and also absorption due to methane (Brogi et al. 2018). Beyond these two planets, we now have a number of transiting gas giants that have revealed their atmospheric make-up (e.g. GJ 3470 b, Nascimbeni et al. 2013; WASP-12 b, Kreidberg et al. 2015; MASCARA-2 b/KELT-20 b, Casasayas-Barris et al. 2019; KELT-9 b, Turner et al. 2020).

Although we have learned a great deal about gas giants, the vast majority of what we know applies only to the hottest subset, those closest to their stars that are heavily irradiated. The equilibrium temperatures of these hot Jupiters are generally >1000 K, and therefore their atmospheric chemistries and physical properties are very different from those on longer period orbits, like Jupiter in our Solar system. The population of longer period transiting planets is growing (e.g. HATS-17 b, Brahm et al. 2016; Kepler-538 b, Mayo et al. 2019; EPIC 249893012 c and d, Hidalgo et al. 2020), particularly since the introduction of *TESS* that finds transits orbiting significantly brighter stars than *Kepler* or *K2*, and across the whole sky (e.g. HD 1397 b, Brahm et al. 2019; TOI-667 b, Jordán et al. 2019; HD 21749 b & c, Dragomir et al. 2019, LTT 9779 b, Jenkins et al. 2020). However, despite these gains, we still know of not many known transiting planets with orbital periods greater than 40 d, orbiting stars bright enough for detailed atmospheric characterization ($V < 9$).

Here we introduce HD 95338 b, a super-Neptune planet detected using precision RVs as part of the Planet Finder Spectrograph (PFS; Crane, Shtetman & Butler 2006; Crane et al. 2008, 2010) long-term planet search project, and which we found to transit after analysing the *TESS* light curve. HD 95338 b is the first planet candidate from *TESS* discovered with a period larger than 27 d (the time baseline of the *TESS* data series). Therefore, it is the first single-transit planet detected from the *TESS* mission.

2 SPECTROSCOPIC OBSERVATIONS

High-precision Doppler measurements of HD 95338 were acquired using PFS mounted on the 6.5-m Magellan II (Clay) telescope at Las Campanas Observatory, and the High Accuracy Radial velocity Planet Searcher (HARPS; Pepe et al. 2002) installed on the ESO 3.6-m telescope at La Silla Observatory.

2.1 PFS

Observations were carried out using PFS between 2010 February 26 and 2018 May 25, as part of the Magellan Exoplanet Long Term Survey (LTS). PFS uses an iodine cell for precise RV measurements and it delivers a resolving power of $R \sim 80\,000$ in the iodine region when observing with the 0.5×2.5 arcsec² slit. Iodine-free template observations were acquired with the 0.3×2.5 arcsec² slit at a resolving power of $R \sim 127\,000$. Fifty two observations were acquired using an average of 540 s of exposure time, yielding a mean RV uncertainty of 1.13 m s^{-1} and a median signal-to-noise ratio (S/N) ~ 144 .

Table 1. PFS1 radial velocities of HD 95338.

BJD (−2450000)	RV (m s^{-1})	σ RV (m s^{-1})	S (dex)	σS (dex)
5253.72066	1.806	1.191	0.2450	0.012
5256.80073	3.796	1.186	0.1867	0.012
5342.53484	−2.873	1.114	0.3596	0.012
5348.50146	0.620	1.317	0.2815	0.012
5349.52059	−1.081	1.371	0.2713	0.012
5588.85377	2.115	0.988	0.1724	0.012
5663.60446	5.616	1.178	0.1918	0.012
5959.79501	−3.994	1.019	0.2402	0.012
6284.83957	−6.118	0.836	0.2481	0.012
6291.83583	−7.558	0.829	0.1590	0.012
6345.74970	−6.404	1.179	0.2418	0.012
6355.71078	−2.553	1.206	0.3401	0.012
...

Notes. This table is published in its entirety in a machine-readable format. A portion is shown here for guidance regarding its form and content.

Table 2. PFS2 radial velocities of HD 95338.

BJD (2450000)	RV (m s^{-1})	σ RV (m s^{-1})	S (dex)	σS (dex)
8471.81505	5.205	0.931	0.1644	0.008
8471.82063	3.733	0.892	0.1659	0.008
8473.82297	2.519	0.918	0.1690	0.008
8473.82677	2.613	0.910	0.1705	0.008
8474.83964	2.712	0.869	0.1770	0.008
8474.84350	1.512	0.839	0.1654	0.008
8475.84374	1.324	0.751	0.1586	0.008
8475.84752	0.202	0.784	0.1609	0.008
8476.82523	−2.224	0.797	0.1631	0.008
8476.82897	1.295	0.785	0.1571	0.008
8479.84682	−3.814	0.813	0.1623	0.008
...

Notes. This table is published in its entirety in a machine-readable format. A portion is shown here for guidance regarding its form and content.

PFS was upgraded with a new CCD detector in 2017. The new CCD is a $10\text{k} \times 10\text{k}$ sensor and has smaller pixels, which improves the line sampling in the spectra. In addition, regular LTS stars are now observed using the 0.3×2.5 arcsec² slit, therefore improving the resolution. The data using this new setup are labelled as PFS2 and include 31 observations. For this upgraded setup, the mean exposure time used was 485 s for each observation, giving rise to a mean RV uncertainty of 0.87 m s^{-1} for a median S/N ~ 74 . The radial velocities are computed with a custom pipeline following the procedure outlined by Butler et al. (1996). They are listed in Tables 1 and 2.

The spectral wavelength range in PFS covers the Ca II H&K lines, enabling the possibility of deriving S -indices to monitor the stellar chromospheric activity. S -indices are derived using the prescription outlined by Baliunas, Sokoloff & Soon (1996) and Boisse et al. (2011). In general, authors determine their S -index errors based on photon noise on the CCD (Boisse et al. 2011; Lovis et al. 2011; Jenkins et al. 2017). In our case, however, doing so can grossly underestimate the real error, reporting <1 per cent or smaller, as they are probably dominated by instrumental systematics (e.g. wavelength calibration, normalization errors). To avoid any bias to unrealistic

Table 3. TERRA Radial Velocities of HD 95338.

BJD (2450000)	RV (m s ⁻¹)	σ RV (m s ⁻¹)	S (dex)	σS (dex)
8262.52210	-2.347	0.963	0.1568	0.0016
8263.58809	-2.716	0.555	0.1642	0.0011
8264.56962	-2.820	0.775	0.1637	0.0014
8265.60191	-2.412	0.677	0.1672	0.0012
8266.54165	-4.199	1.105	0.1520	0.0018
8429.84914	0.0	0.706	0.1580	0.0011
8430.83705	1.651	0.712	0.1606	0.0009
8576.69728	12.654	1.156	0.1584	0.0016
8577.79238	14.113	1.479	0.1504	0.0023
8578.71982	11.102	0.853	0.1564	0.0013
8579.70958	11.115	0.790	0.1605	0.0012

error estimation, we assumed a homogeneous 5 per cent error bar estimated from the rms of the S -index series.

2.2 HARPS

Eleven observations using HARPS were acquired between 2018 May 24 and 2019 April 6 from program IDs 0101.C-0497, 0102.C-0525, and 0103.C-0442 (PI: Díaz), in order to confirm the signal found in PFS data and also to constrain the orbital parameters of the planet candidate. The observations were carried out using simultaneous Thorium exposures with a fixed exposure time of 900 s, reaching a mean S/N of ~ 67 at 5500 Å. We re-processed the observations with the TERRA software (Anglada-Escudé & Butler 2012), where a high S/N template is constructed by combining all the observations that pass a threshold S/N cutoff, and then the RVs are computed by a χ^2 -fitting process relative to this template. The mean RV uncertainty we get from this analysis is ~ 0.89 m s⁻¹. TERRA also provides a computation of the S -indices and their uncertainties. These along with the RVs are listed in Table 3.

3 STELLAR PARAMETERS

We derived [Fe/H], T_{eff} , age, mass, radius, $\log g$, and $v \sin i$ using the spectral classification and stellar parameter estimation package *species* (Soto & Jenkins 2018), previously used in, e.g. Díaz et al. (2018, 2020). In short, *species* derives T_{eff} , $\log g$, [Fe/H], and microturbulence by measuring the equivalent widths (EWs) of a list of neutral and ionized iron lines, and then using MOOG (Snedden 1973) to solve the radiative transfer equation in the stellar interior, along with ATLAS9 model atmospheres (Castelli & Kurucz 2004). The adopted values for the atmospheric parameters are those for which no correlation is found between the individual iron abundance and the line excitation potential, nor the reduced EWs (EW/λ), and the average abundance for the Fe I and Fe II lines is the same. The EWs used in this work were measured by fitting Gaussian-shaped profiles to the absorption lines through the `EWComputation`¹ module in *species*. Details of the fitting procedure will appear in Soto et al. (in preparation). We produced a high S/N, stacked spectrum from HARPS observations to be used for the precise computation of the EWs. Physical parameters like mass and age are found by interpolation through a grid of MIST models (Dotter 2016), using the `isochrones` PYTHON package (Morton 2015).

¹ Available at <https://github.com/msotov/EWComputation>.

Table 4. Stellar Parameters of HD 95338.

Parameter	Value	Source
TESS name	TIC 304142124	
RA (J2000)	10:59:26.303	SIMBAD
Dec. (J2000)	-56:37:22.947	SIMBAD
TESS	7.8436 \pm 0.0006	ExoFOP ^a
H	6.729 \pm 0.037	2MASS
J	7.098 \pm 0.024	2MASS
K_s	6.591 \pm 0.017	2MASS
V	8.604 \pm 0.012	SIMBAD
B	9.487 \pm 0.013	SIMBAD
G	8.3821 \pm 0.0003	<i>Gaia</i>
RP	7.8017 \pm 0.0013	<i>Gaia</i>
BP	8.8464 \pm 0.001	<i>Gaia</i>
W1	6.553 \pm 0.071	WISE
W2	6.578 \pm 0.023	WISE
Parallax (mas)	27.0553 \pm 0.0499	<i>Gaia</i> (Zinn et al. 2019)
Distance (pc)	36.97 ^{+0.02} _{-0.03}	This work
Spectral type	K0.5V	This work (<i>ariadne</i>)
Mass (M_{\odot})	0.83 ^{+0.02} _{-0.02}	This work (<i>ariadne</i>)
Radius (R_{\odot})	0.87 ^{0.04} _{0.04}	This work (<i>ariadne</i>)
Age (Gyr)	5.08 \pm 2.51	This work (<i>species</i>)
A_V	0.073 ^{+0.012} _{-0.015}	This work (<i>ariadne</i>)
Luminosity (L_{\odot})	0.49 \pm 0.01	Anderson & Francis (2012)
T_{eff} (K)	5212 ⁺¹⁶ ₋₁₁	This work (<i>species</i>)
[Fe/H]	0.04 \pm 0.10	This work (<i>species</i>)
$\log g$	4.54 \pm 0.21	This work (<i>species</i>)
$v \sin i$ (km s ⁻¹)	1.23 \pm 0.28	This work (<i>species</i>)
v_{mac} (km s ⁻¹)	0.97 \pm 0.41	This work (<i>species</i>)

Note. ^a<https://exofop.ipac.caltech.edu/tess/>.

Finally, macroturbulence and rotation velocity were computed using temperature relations and fitting synthetic profiles to a set of five absorption lines (see Soto & Jenkins 2018 for more details).

Then we performed a spectral energy distribution (SED) fit to publicly available catalogue photometry shown in Table 4 using the values found by *species* as priors.

The SED fit was done with *ariadne*, a PYTHON tool designed to automatically fit archival photometry to atmospheric model grids. Phoenix v2 (Husser et al. 2013), BT-Settl, BT-Cond (Allard, Homeier & Freytag 2012), BT-NextGen (Hauschildt, Allard & Baron 1999; Castelli & Kurucz 2004) and Kurucz (1993) stellar atmosphere models were convolved with different filter response functions – *UBVRI*; 2MASS *JHK_s* (Skrutskie et al. 2006); SDSS *ugriz*; WISE W1 and W2; *Gaia G, RP, and BP* (*Gaia* Collaboration et al. 2016, 2018); Pan-STARRS *girwyz*; Strömgren *uvby*; GALEX NUV and FUV; *TESS*; *Kepler*; and NGTS – to create six different model grids. We then model each SED by interpolating the model grids in the $T_{\text{eff}}\text{--}\log g\text{--}[\text{Fe}/\text{H}]$ space. The remaining parameters are distance, radius, extinction in the V band, and individual excess noise terms for each photometry point in order to account for possible underestimated uncertainties or variability effects. We set priors for T_{eff} , $\log g$, and [Fe/H] from the *species* results; for the radius, we took *Gaia* DR2 radius values as prior, and for the distance, we used the *Gaia* parallax as priors (after applying the $-52.8 \pm 2.4 \mu\text{as}$ correction from Zinn et al. 2019) and then we treated it as a free parameter in the fitting routine. We limited the A_V to a maximum of 4.243 taken from the re-calibrated SFD Galaxy dust map (Schlegel, Finkbeiner & Davis 1998; Schlafly & Finkbeiner 2011). Each excess noise parameter has a zero mean normal distribution as the prior,

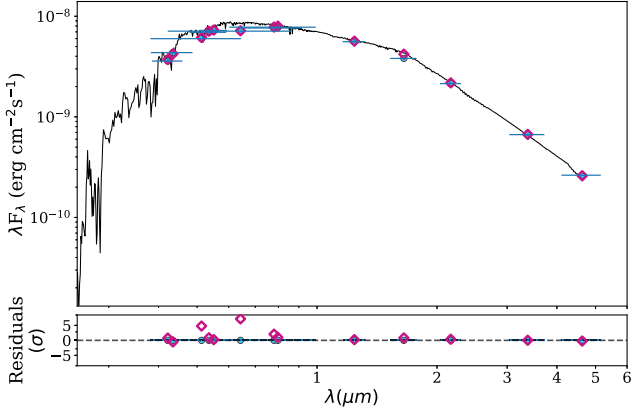


Figure 1. Top panel: best-fitting BT-Cond SED model. Blue points show the photometry and magenta diamonds show the synthetic photometry. Horizontal error bars show the width of the filter bandpass. Bottom panel: residuals of the fit, normalized to the photometry errors.

with the variance equal to five times the size of the reported uncertainty. We then performed the fit using *dynesty*'s nested sampler (Speagle 2019) to sample the posterior parameter space, obtaining the Bayesian evidence of each model and the marginalized posterior distribution for each fitted parameter as a by-product. Finally, we averaged the posterior samples of each model, weighting each sample by its normalized evidence. To plot the SED, we selected the model grid with the highest evidence to calculate the synthetic photometry and overall model (Fig. 1). We note the residuals from Fig. 1 are normalized to the error of the photometry. In the case of precise photometry, e.g. *Gaia*, the residuals show a relatively high scatter. A more detailed explanation of the fitting procedure, accuracy, and precision of *ariadne* can be found in Vines & Jenkins (in preparation).

4 DETECTION FROM RVs

We began examining the RV data by using the traditional periodogram analysis approach to look for any periodicities embedded in the data. We used the generalized version (Zechmeister & Kürster 2009) of the Lomb–Scargle periodogram (Lomb 1976; Scargle 1982, hereafter GLS). Fig. 2 shows the initial RV-only analysis where the signal at 55 d is clearly identified from the combined radial velocities. From this analysis, we informed the following modelling process.

We modelled the radial velocities of HD 95338 following the same procedure defined in Tuomi et al. (2014) and performed in Jenkins & Tuomi (2014) and Díaz et al. (2018) with some slight variations in our model. We define the global model as follows:

$$y_{i,j} = \hat{y}_{i,j} + \epsilon_{i,j} + \eta_{i,j}, \quad (1)$$

where

$$\hat{y}_{i,j} = \gamma_j + f_k(t_i) \quad (2)$$

is the deterministic part of the model composed of an offset γ_j for data set j and the Keplerian component,

$$f_k(t_i) = \sum_{m=1}^{N_p} K_m [\cos(\omega_m + v_m(t_i)) + e_m \cos(\omega_m)], \quad (3)$$

which is a function that describes a m -Keplerian model, where K_m is the velocity semiamplitude, ω_m is the argument of periapsis of the

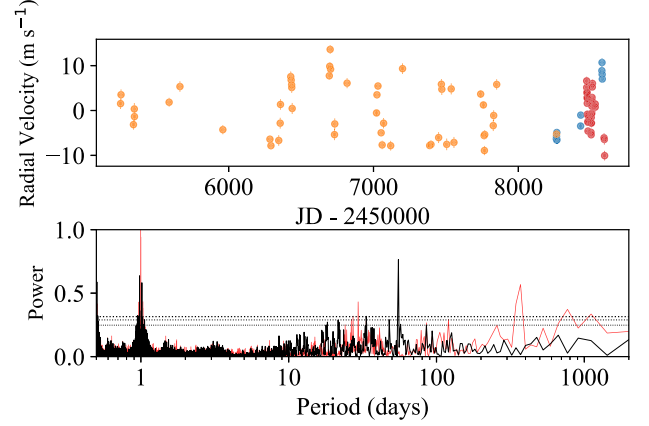


Figure 2. Top panel: RV time series for HD 95338 obtained with PFS1 (orange), PFS2 (red), and HARPS (blue). Bottom panel: GLS periodogram for the combined radial velocities. Each data set has been corrected by their respective velocity zero-point, estimated from the mean of the time series. Horizontal lines, from the bottom to top panels, represent the 10, 1, and 0.1 per cent significance thresholds levels estimated from 5000 bootstraps with replacement on the data. The periodogram in red shows the window function for the time series.

star's orbit with respect to the barycentre, v_m is the true anomaly at the time of the planetary transit, and e_m is the eccentricity for the m th planet. v_m is also a function of the orbital period and the mean anomaly $M_{0,m}$, measured at time $T_0 = 2455\,253.72\,066$.

The stochastic component in the RV data is modelled using a moving average (MA) approach:

$$\eta_{i,j} = \sum_{l=1}^q \phi_{j,l} \exp\left\{-\frac{|t_{i-l} - t_i|}{\tau_j}\right\} (v_{i-l,j} - \hat{y}_{i-l,j}), \quad (4)$$

where $\phi_{j,l}$ represents the amplitude of the q th-order MA model, and τ_j is the time-scale of the MA(q) model for the j th instrument. The range of τ_j is determined according to the data time-span and cadence. Thus, $\tau_{\max} = t_{\max} - t_{\min}$, where t_{\max} and t_{\min} are the maximum and minimum values of the time-span of the combined set, respectively. Finally, $\tau_{\min} = \min\{t_2 - t_1, t_3 - t_2, \dots, t_N - t_{N-1}\}$, represents the minimum difference between two epochs and N is the total number of epochs. The white noise term in equation (1) is denoted by $\epsilon_{i,j}$, where we assume that there is an excess white noise (jitter) in each data set with a variance of σ_j such that $\epsilon_{i,j} \sim \mathcal{N}(0, \sigma_i^2 + \sigma_j^2)$, where σ_i and σ_j are the uncertainties associated with the measurement $y_{i,j}$ and jitter for the j th data set, respectively.

4.1 Posterior samplings and signal detection

In order to estimate the posterior probability of the parameters in the model, given the observed data, we use Bayes' rule:

$$P(\theta | y) = \frac{P(y | \theta) P(\theta)}{\int P(y | \theta) P(\theta) d\theta}, \quad (5)$$

where $P(y | \theta)$ is the likelihood function and $P(\theta)$ corresponds to the prior. The denominator is a normalizing constant such that the posterior must integrate to unity over the parameter space. For our model, we choose the priors for the orbital and instrumental parameters as listed in Table 5.

For a given model, we sample the posterior through multiple tempered (hot) MCMC chains to identify the global maximum of the posterior. We then use non-tempered (cold) chains to sample the

Table 5. Prior selection for the parameters used in the MA analysis.

Parameter	Units	Prior type	Range
Semi-amplitude	m s^{-1}	Uniform	$K \in [0, 100]$
Logarithmic period	d	Uniform	$\ln P \in [\ln(1.1), \ln(10^6)]$
Eccentricity	–	$\mathcal{N}(0, 0.2)$	$e \in [0, 1]$
Longitude of pericentre	rad	Uniform	$\omega \in [0, 2\pi]$
Mean anomaly	rad	Uniform	$M_0 \in [0, 2\pi]$
Jitter	m s^{-1}	Uniform	$\sigma_J \in [0, 100]$
Smoothing time-scale	d	Uniform	$\tau_j \in [\tau_{\min}, \tau_{\max}]$ (see the text)
MA amplitude	–	Uniform	$\phi_j \in [0, 1]$

global maximum found by the hot chains. The procedure is similar to that previously done in Díaz et al. (2018) with the difference that here our MA model includes a correlated (red) noise component, but it does not include explicit correlations with activity indicators because it would introduce extra noise, although it might remove some activity signals (see e.g. Feng et al. 2019b). We explore the correlations between activity indices and radial velocities in Section 5. From the posterior samples, we infer the parameter at the mean value of the distribution and we report the uncertainties from the standard deviation of the distribution. This approach is also explained in detail in Feng et al. (2019a). To select the optimal noise model, we calculate the maximum likelihood for an MA model using the Levenberg–Marquardt (LM) optimization algorithm (Levenberg 1944; Marquardt 1963).

We define the Bayes factor (BF) comparing two given models, \mathcal{M}_k and \mathcal{M}_{k-1} , as

$$\ln B_{k,k-1} = \ln P(y|\mathcal{M}_k) - \ln P(y|\mathcal{M}_{k-1}). \quad (6)$$

We calculate $\ln(\text{BF})$ for $\text{MA}(q+1)$ and $\text{MA}(q)$. If $\ln(\text{BF}) < 5$, we select $\text{MA}(q)$, according to equation (6). If $\ln(\text{BF}) \geq 5$, we select $\text{MA}(q+1)$ and keep increasing the order of the MA model until the model with the highest order passing the $\ln(\text{BF}) \geq 5$ criterion is found. Considering that the Bayesian information criterion (BIC) is a good criterion for signal selection (Kass & Raftery 1995; Feng et al. 2016), we convert BIC into BF according to the formula given by Feng et al. (2016).

Our MCMC runs gave rise to the posterior histograms shown in Fig. 3, where the period, amplitude, and minimum mass (and the remaining orbital parameters) show Gaussian distributions centred on their respective mean values.

From the posterior distributions for T_{peri} (see Fig. 3), we obtain $T_c = 2458\,585.929 \pm 0.840$, which turns out to be well in agreement, within uncertainties, with the ephemeris from the *TESS* photometry, $T_{c, \text{TESS}} = 2458\,585.279$ (see Table 8). The posterior mean values for the RV-only analysis are listed in Table 6. It is worth noting that the final value for the time-scale of the red noise, τ_j , is not constrained for PFS2 as it did not converge to a unique solution. We choose the best $\text{MA}(q)$ model based on 0-planet + $\text{MA}(q)$ model comparison and thus q is determined based on the assumption that the time correlation in the RV data is totally noise; therefore, q is typically larger than it should actually be. This is the reason why the amplitude and time-scale of $\text{MA}(q)$ models sometimes do not converge after adding Keplerian components which can explain the time correlation in the data better than stochastic red noise models such as MA. Although we can perform a selection of q and number of signals simultaneously, it would be a two-dimensional model selection and is thus time consuming. On the other hand, if a data set only contains white noise and signals, the Keplerian model will be

favoured against the MA model due to the advantage of simultaneous fitting. Compared to previous adoption of a single red noise model such as GP, our approach is more robust to overfitting or underfitting problems.

We note that additional tests were conducted using the Delayed Rejection Adaptive Metropolis algorithm (Metropolis et al. 1953; Haario, Saksman & Tamminen 2001; Haario et al. 2006), as previously done in Tuomi et al. (2014) and Díaz et al. (2018), and we found the results were in full agreement with the MA approach within the uncertainties.

5 STELLAR ACTIVITY AND RV CORRELATIONS

We computed the GLS periodogram of the combined S -indices from PFS1, PFS2, and HARPS (Fig. 4). We do not find statistically significant periods from stellar activity matching the signal of the planet candidate (marked with a vertical line). However, we do see multiple peaks at ~ 1 , ~ 29 , and ~ 150 d above the 1 percent significance threshold. The 1-d period is likely due to the frequency of the sampling in the observations; similarly, the 29-d peak is close to the lunar period. The additional 150-d period could be related to a stellar magnetic cycle, but more data are needed to test this hypothesis. Fig. 5 shows the correlations between the mean-subtracted activity indices in the Mt. Wilson system, S_{MW} , and the radial velocities PFS1 (open triangles), PFS2 (black triangles), and HARPS (orange circles). We note the improvement in the scatter from PFS2 compared to PFS1; new activity indices are comparable to the scatter of those from HARPS, derived using the TERRA software. We see four points that are far off from the mean. We find the Pearson r correlation coefficients for PFS1, PFS2, and HARPS are 0.15, 0.38, and -0.39 , respectively, meaning no significant strong correlations are found ($|r| < 0.5$).

6 PHOTOMETRY

6.1 *TESS* photometry

HD 95338 was observed by the *TESS* (Ricker et al. 2015). We checked the target was observed using the Web *TESS* Viewing Tool (WTV²), as initially the target did not produce an alert on the *TESS* Releases website³ where an overview of table, alerts, and downloadable data is available. We identified a single transit in the *TESS* photometry containing data from Sector 10 using camera 3, observed between 2019 March 26 and April 22.

²<https://heasarc.gsfc.nasa.gov/cgi-bin/tess/webtess/wtv.py>.

³<https://tev.mit.edu/data/>.

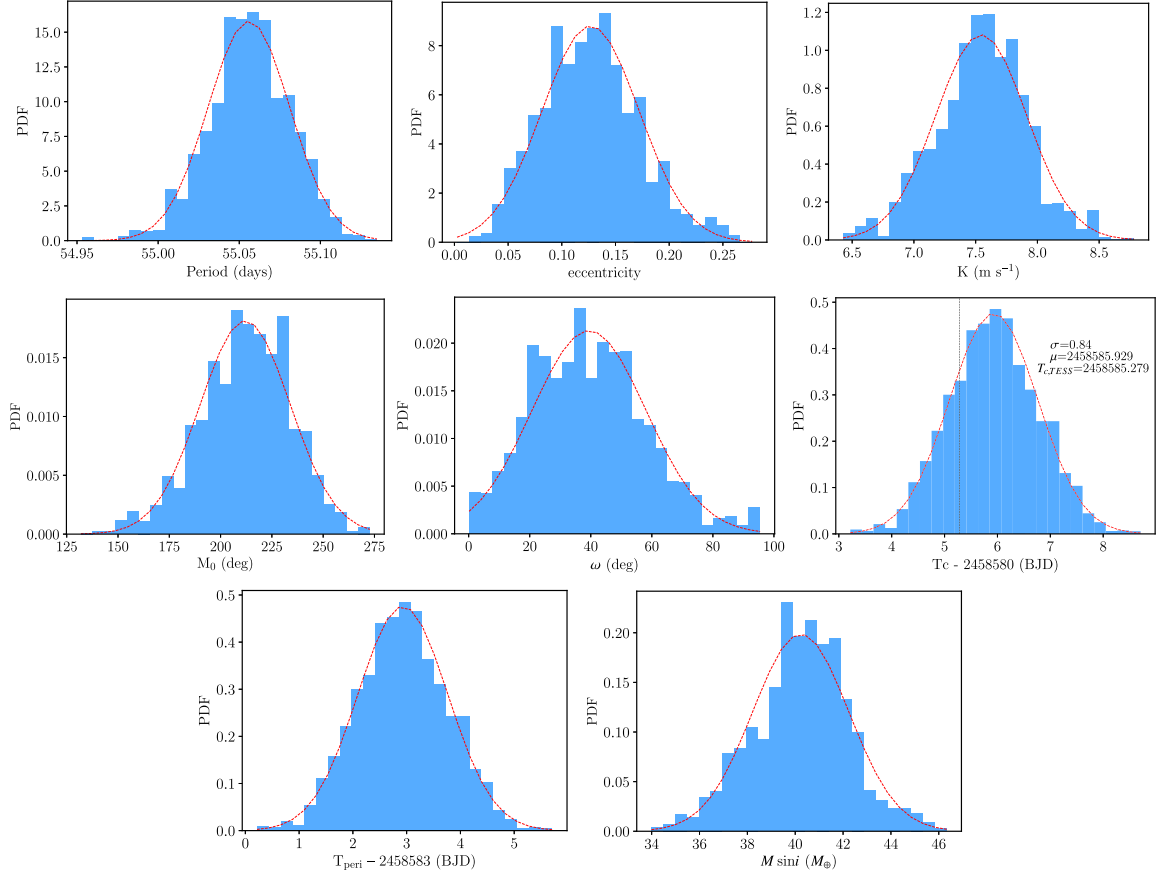


Figure 3. Posterior distributions of the orbital parameters P , e , K , M_0 , ω , T_c , T_{peri} , and minimum mass, respectively, obtained from our RV analysis. Dashed red lines on each plot show a Gaussian fit to the posterior distribution. T_c is derived from the time of pericentre passage values (T_{peri} ; see the text). The vertical black dashed line represents the transit time from the *TESS* light curve. From the histogram, we found a mean value of $T_c = 2458\,585.929$ and $\sigma = 0.84$, which overlaps nicely with the transit time from the light curve, strongly suggesting both signals could originate from the same source.

Table 6. Posterior for the parameters included in the RV-only analysis.

Parameter	Value
P (d)	55.056 ± 0.025
T_{peri} (BJD – 2450000)	8585.2795 ± 0.8384
K (m s^{-1})	7.54 ± 0.37
e	0.127 ± 0.045
ω ($^\circ$)	39.428 ± 18.719
M_0 ($^\circ$)	212.004 ± 21.983
$M \sin i$ (M_\oplus)	40.34 ± 2.01
μ_{PFS1} (m s^{-1})	0.316 ± 0.584
$\sigma_{J,\text{PFS1}}$ (m s^{-1})	1.725 ± 0.818
ϕ_{PFS1}	0.457 ± 0.426
$\ln\tau_{\text{PFS1}}$	3.18 ± 1.10
μ_{PFS2} (m s^{-1})	0.178 ± 0.780
$\sigma_{J,\text{PFS2}}$ (m s^{-1})	0.985 ± 0.532
ϕ_{PFS2}	0.360 ± 0.314
$\ln\tau_{\text{PFS2}}$	0.323 ± 6.895
μ_{HARPS} (m s^{-1})	0.796 ± 0.938
$\sigma_{J,\text{HARPS}}$ (m s^{-1})	1.80 ± 0.87

Notes. MA(1) applied to PFS. White noise applied to HARPS.

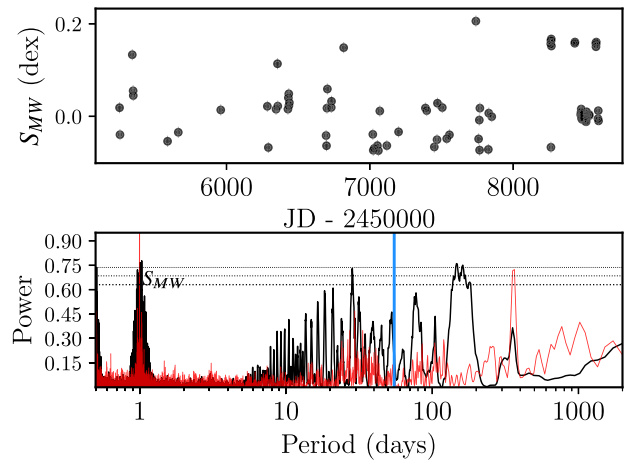


Figure 4. Top panel: time series of combined, mean-subtracted S -indices from HARPS, PFS1, and PFS2. Bottom panel: GLS periodogram of the S -indices. The vertical line shows the position of the 55-d RV signal. Horizontal lines, from the bottom to top panels, represent the 10, 1, and 0.1 percent significance levels estimated from 5000 bootstraps with replacement on the data.

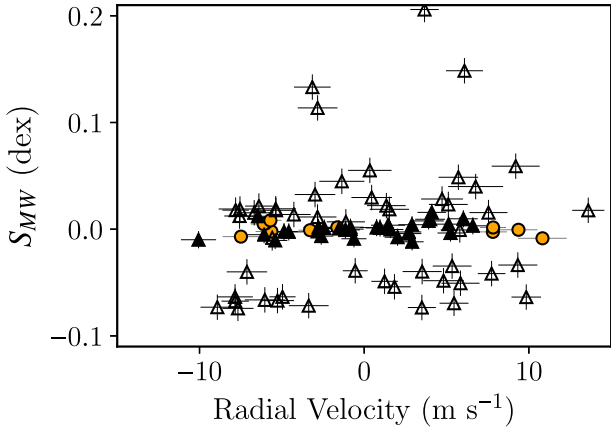


Figure 5. RV correlations versus S -indices from HARPS (circles), PFS1 (triangles), and PFS2 (black triangles).

We extracted the PDCSAP_FLUX 2-min cadence photometry following the same procedures we recently used in Díaz et al. (2020). The PDCSAP_FLUX median-corrected photometry is shown in the top panel of Fig. 6. We then applied a median filter to remove the light-curve variability, in particular on both sides near the transit event. The final flattened light curve is shown in the lower panel of Fig. 6, and it is the transit data that were used throughout all our analyses.

We note that the star is located in a relatively crowded field, as *Gaia* returns 12 sources within an angular separation of 1 arcmin. Given that the pixels in the *TESS* cameras are 21-arcsec wide, this could mean some of the sources would contaminate the aperture. However, the brightest nearby source is $G \sim 18$ mag, which is 12 mag fainter than HD 95338 ($G = 8.38$). Converted into flux, this companion is ~ 7000 times fainter than HD 95338. From a preliminary inspection and analysis of the light curve, we estimated a transit depth of $\sim 2000 \pm 500^4$ ppm. Therefore, the difference in flux would cause a depth of ~ 100 ppm, which we find to be negligible compared to the transit depth.

Recent work by Sandford et al. (2019) has shown the use of single-transit light curves to estimate orbital periods based on precise parallaxes from *Gaia*. While their work focused on *K2* data, we can apply the same methodology to our *TESS* light curve, since we also know the transit depth, and we can calculate the scaled semimajor axis and stellar density from the combination of the *ariadne* results and the high-resolution spectra. We recall equations (1) and (2) from Sandford et al. (2019):

$$P^2 = \frac{3\pi}{G} \left(\frac{a}{R_\star} \right)^3 \rho_\star^{-1}, \quad (7)$$

$$\sigma_P = \frac{P}{2} \sqrt{\left(\frac{\sigma_{\rho_\star}}{\rho_\star} \right)^2 + \left(\frac{3\sigma_{\frac{a}{R_\star}}}{\frac{a}{R_\star}} \right)^2}, \quad (8)$$

which yield the orbital period (and the associated error) of a single transit using Kepler's third law and assuming circular orbits, where G is the gravitation constant, (a/R_\star) corresponds to the scaled semimajor axis measured directly from the shape of the transit, and ρ_\star is the stellar density that must come from an independent analysis. In our case, we used the stacked spectra acquired with HARPS, and from our spectra classification analysis with *species* combined

with the SED fit, we find a stellar density of $\rho_\star = 1.68^{+0.45}_{-0.23} \text{ g cm}^{-3}$. We estimate $(a/R_\star) = 58.06^{+1.39}_{-2.48}$ from the transit seen in the *TESS* light curve. Then, using equations (1) and (2) from Sandford et al. (2019), we get an estimate for an orbital period of 47 ± 9 d for the single transit observed by *TESS* being consistent within the uncertainties to the period of the signal found in the RV data.

6.2 ASAS photometry

In an attempt to search for additional sources of periodicity, we used data from the All Sky Automated Survey (ASAS; Pojmanski 1997). Fig. 7 shows the photometry time series consisting on 625 measurements from 2000 December 7 to 2009 December 3. We selected the best quality data, flagged as 'A' or 'B'. We used the GLS periodogram to search for signals after filtering the highest quality data from outliers, and found no statistically significant periods that could be attributed to the stellar rotation period, due in part to the size of the typical uncertainty in the ASAS photometry.

In order to address how often we could recover a prediction for the transit centroid, T_c , which has an uncertainty of 1.5 per cent of the orbital period or better, just as we see for HD 95338 b, we simulated 10^6 systems with a single planet and random orbital parameters. We consider that all the random systems transit their host stars and we used flat priors for the distribution of longitude of pericentre, ω , and for the eccentricity. For the distribution of orbital periods, we used the broken power law presented in Mulders et al. (2018), where the break occurs at $P_b = 10$ d. For shorter periods, the probability is written as $(P/P_b)^{1.5}$, while for longer periods, the probability is unity. For each system, we generated the remaining orbital parameters according to standard equations for the orbital parameters, and used these to predict T_c (see Section 4). We find that ~ 9 per cent of the systems sampled randomly fulfill this criterion.

If the agreement between the RV prediction and transit T_c found for HD 95338 b is just a statistical fluke, then this means there are more planets in the system, since another body must give rise to the transit. The probability of 9 per cent does not consider this possibility. For that to be the case, we should also normalize by the fraction of Neptunes that are found in multiple systems. Although this value is uncertain, and may actually be ~ 100 per cent, we can at least estimate it using a literature search. To do this, we retrieved the number confirmed Neptunes with known companions detected by the transit method by *Kepler/K2* from the *exoplanet.eu*⁵ catalogue in a mass range between 10 and $45 M_\oplus$. We find that the number of these multisystems is 19 out of a total of 65, which corresponds to a fraction of ~ 29 per cent. This leads to a final probability of ~ 3 per cent, meaning it is highly unlikely that we have observed the configuration we find for HD 95338 b if the orbital parameters are randomly distributed. Even if Neptunes are indeed found to exist exclusively in multiplanet systems, there is still a 91 per cent probability that the RV detected companion and the *TESS*-detected companion are the same object.

7 JOINT ANALYSIS

We performed a joint fit of the photometry and radial velocities (Tables 1–3) using the *juliet* package (Espinoza, Kossakowski & Brahm 2019) in order to estimate the orbital parameters for the system. To model the photometry, *juliet* uses the *batman* package (Kreidberg 2015) while the radial velocities are modelled using

⁴<https://exofop.ipac.caltech.edu/tess/target.php?id=304142124>.

⁵<http://exoplanet.eu/catalog/>.

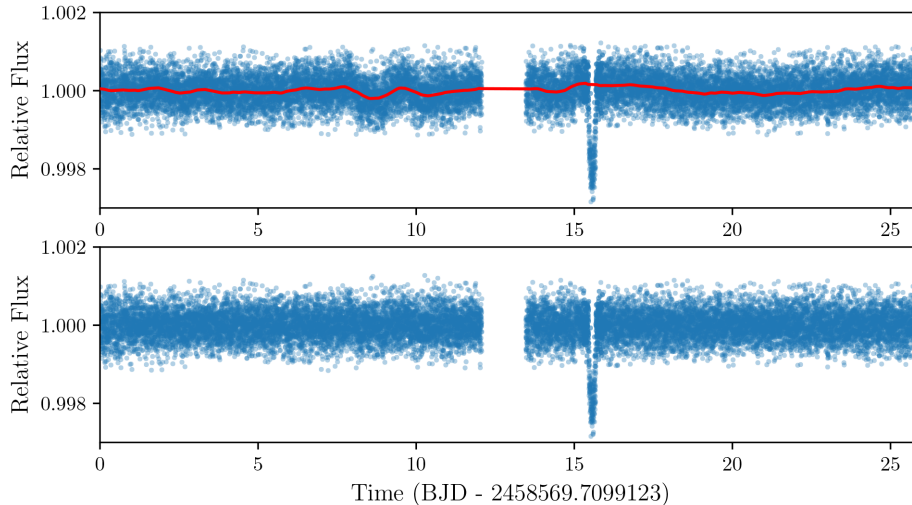


Figure 6. Top panel: PDC_SAP light curve for HD 95338 from *TESS* Sector 10 showing the single transit. The red solid curve on top of the photometry shows a median filter applied to remove variability. Bottom panel: median-filter-corrected PDC_SAP *TESS* light curve for HD 95338.

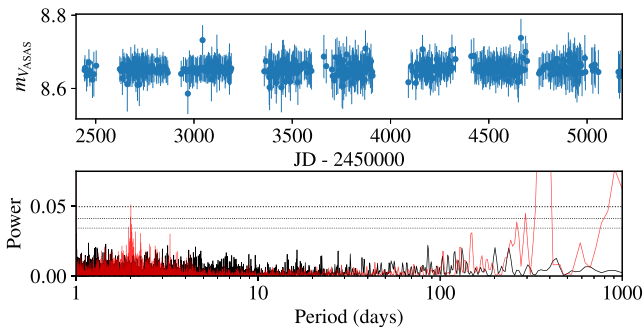


Figure 7. GLS periodogram for the ASAS V-band photometry. Horizontal lines mark the position of the 10, 1, and 0.1 per cent FAP threshold levels, from the bottom to top panels, respectively. A peak close to ~ 90 d is seen in the power spectrum; however, it is below any FAP threshold and cannot be considered as statistically significant.

`radvel` (Fulton et al. 2018). We then sampled the parameter space using the `dynesty`-nested sampler (Speagle 2019) to compute posterior samples and model evidences. The parameters for the joint model were set according to Table 7. We treated the eccentricity as a free parameter motivated by our finding from the RV-only analysis, suggesting the eccentricity was different from zero. The resultant value was in agreement with the one from our previous analysis. The RV semiamplitude prior was chosen to be flat between 1 and 100 to explore a wider range of amplitudes and not only values centred around the semiamplitude found in the RV-only analysis. The jitter terms for PFS1, PFS2, and HARPS were set using a Jeffreys prior over two orders of magnitude (0.1 to 10 m s^{-1}), resulting in excess RV noise of 2.3, 1.3, and 1.6 m s^{-1} , respectively. For the orbital period, we used a Jeffreys prior over two orders of magnitude, from 1 to 100 d. The time of transit (T_c) was derived from the time of pericentre passage (T_{peri}) as discussed in Section 4.1. However, we also chose an uninformative prior using the whole range of the RV baseline.

For the photometry parameters, we used the efficient sampling for the transit depth (p) and impact parameter (b) described in Espinoza

(2018), which allows only physically plausible values in the (b , p) plane to be sampled via the r_1 and r_2 coefficients, according to the description of Kipping (2013) for two parameter laws. As a result we obtained a planet mass of $42.44^{+2.22}_{-2.08} M_{\oplus}$, consistent with a super-Neptune, with a radius of $3.89^{+0.19}_{-0.20} R_{\oplus}$, which translates into a relatively high density of $3.98^{+0.62}_{-0.64} \text{ g cm}^{-3}$ for this planet. We note here we did not use GPs nor MA as in the RV-only analysis, so the residuals shown in Fig. 8 (right-hand panel) are really the full residuals from a pure Keplerian model including instrumental jitter.

8 ADDITIONAL SIGNALS

We searched for additional signals by analysing the residuals from the one-planet fit using same MA approach described in Section 4. Fig. 9 shows the Bayes Factor Periodogram (BFP; Feng, Tuomi & Jones 2017) of the residual radial velocities for a one-planet model. For these data, we do not find evidence for additional statistically significant signals present in the system after removing the 55-d planet signal. However, we do see a periodic signal at ~ 46 d in the residual BFP, but we cannot reach any conclusion at this moment as the signal is below the detection threshold of $\ln(\text{BF}) > 5$ to be considered as significant. It can be related to the activity of the star, based on what we see in the periodogram analysis of the stellar activity indicators where we see some hints of periodicities around 30–40 d. Additional spectroscopic data will help to confirm or rule out additional signals.

9 DISCUSSION

To better understand the composition of HD 95338 b, we have constructed interior structure models matched to its observed mass, radius, and orbital parameters. These models are explained in detail in Thorngren et al. (2016); briefly, they solve the equations of hydrostatic equilibrium, conservation of mass, and the material equation of state (EOS) to determine the radius of a well-mixed planet. The EOS used were Chabrier, Mazevet & Soubiran (2019) for H/He and a 50–50 ice–rock mixture from ANEOS (Thompson 1990) for the metals. Giant planets gradually cool by radiating

Table 7. Priors used on the joint analysis of HD 95338.

Parameter name	Prior	Units	Description
ρ_*	$\mathcal{N}(1685, 30)$	kg m^{-3}	Stellar density
Parameters for planet b			
P_b	$\mathcal{J}(1, 100)$	d	Orbital period
$T_{c,b} - 2457000$	$\mathcal{U}(1000, 1100)$	d	Time of transit centre
$r_{1,b}$	$\mathcal{U}(0, 1)$	–	Parametrization for p and b^a
$r_{2,b}$	$\mathcal{U}(0, 1)$	–	Parametrization for p and b^a
K_b	$\mathcal{U}(1, 100)$	m s^{-1}	Radial-velocity semi-amplitude
e_b	$\mathcal{U}(0, 1)$	–	eccentricity
ω_b	$\mathcal{U}(0, 359.)$	$^\circ$	Argument of periastron
Parameters for <i>TESS</i>			
D_{TESS}	1.0 (fixed)	–	Dilution factor for <i>TESS</i>
M_{TESS}	$\mathcal{N}(0, 1000)$	ppm	Relative flux offset for <i>TESS</i>
$\sigma_{w,\text{TESS}}$	$\mathcal{J}(0.1, 100)$	ppm	Extra jitter term for <i>TESS</i> light curve
$q_{1,\text{TESS}}$	$\mathcal{U}(0, 1)$	–	Quadratic limb-darkening parametrization
$q_{2,\text{TESS}}$	$\mathcal{U}(0, 1)$	–	Quadratic limb-darkening parametrization
RV instrumental parameters			
μ_{PFS1}	$\mathcal{N}(0, 10)$	m s^{-1}	RV zero-point (offset) for PFS1
$\sigma_{w,\text{PFS1}}$	$\mathcal{J}(0.1, 10)$	m s^{-1}	Extra jitter term for PFS1 radial velocities
μ_{PFS2}	$\mathcal{N}(0, 10)$	m s^{-1}	RV zero-point (offset) for PFS2
$\sigma_{w,\text{PFS2}}$	$\mathcal{J}(0.1, 10)$	m s^{-1}	Extra jitter term for PFS2 radial velocities
μ_{HARPS}	$\mathcal{N}(0., 10)$	m s^{-1}	RV zero-point (offset) for HARPS
$\sigma_{w,\text{HARPS}}$	$\mathcal{J}(0.1, 10)$	m s^{-1}	Extra jitter term for HARPS radial velocities

Note. ^a We used the transformations outlined in Espinoza (2018).

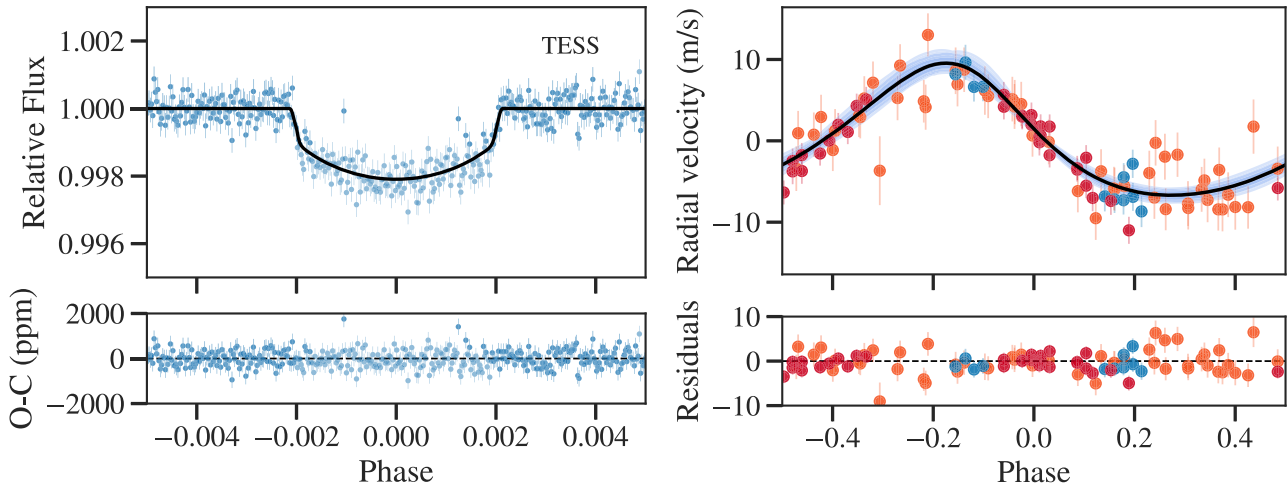


Figure 8. Left-hand panel: *TESS* light curve phase-folded to the period of 55 d. The solid line shows the model for the transit. The bottom panel shows the residuals. Right-hand panel: phase-folded radial velocities from PFS1 (orange), HARPS (blue), and PFS2 (red) where the jitter has been added to the error bars. The solid black line represents the Keplerian model from the joint fit with *juliet*. The orbital parameters for the system are listed in Table 8.

away the residual heat left over from their initial formation, which we regulated using the atmosphere models of Fortney, Marley & Barnes (2007) to evolve the planets through time. Finally, we used the Bayesian retrieval framework from Thorngren & Fortney (2019) to infer the bulk metallicities consistent with the planet parameters. The planet is cool enough that no anomalous heating effect should be present. The composition is consistent with that of ice (Fig. 10), which is to say a mixture of ammonia, water, and methane without regard for the actual state of matter. Indeed, the ices in this planet would be mostly supercritical fluids, with possibly plasma near the core, and maybe a small amount of gaseous

water in the atmosphere. The only solid material would be iron and rocks.

Our models show that to reproduce the planet’s high bulk density ($\rho_p = 3.98^{+0.62}_{-0.64} \text{ g cm}^{-3}$), a metallicity of $Z = 0.90 \pm 0.03$ was required (see Fig. 11). As such, it is among the most metal-rich planets of this mass range, and raises questions about how the planet formation process can gather so much metals without also accreting more H/He. While extreme, this is not truly an outlier: Other planets in this mass range are also found to have high metallicities (see Thorngren et al. 2016), including Kepler-413 b ($M_p = 0.21 M_J$, $Z \simeq 0.89$; Kostov et al. 2014) and K2-27 b ($M_p = 0.09 M_J$, $Z \simeq 0.84$; Van

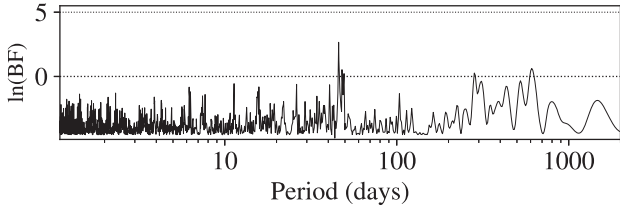


Figure 9. BFP of the residuals for the one-planet model from our joint fit with `juliet`. No statistically significant signals are seen after subtracting the 55-d period. There is a peak in the power spectrum around signal around 46 d; however, it is below our detection threshold $\ln(\text{BF}) > 5$.

Table 8. Planetary properties for HD 95338 b.

Property	Value
Fitted parameters	
ρ_{\star} (kg m^{-3})	$1686.537^{+29.810}_{-29.993}$
P (d)	$55.087^{+0.020}_{-0.020}$
T_c (BJD – 2450000)	$8585.2795^{+0.0006}_{-0.0006}$
a/R_{\star}	$64.676^{+0.381}_{-0.384}$
b	$0.430^{+0.070}_{-0.113}$
K (m s^{-1})	$8.17^{+0.42}_{-0.39}$
i_p ($^{\circ}$)	$89.57^{+0.09}_{-0.05}$
e	$0.197^{+0.029}_{-0.024}$
ω ($^{\circ}$)	$23.42^{+11.53}_{-11.99}$
Derived parameters	
M_p (M_{\oplus})	$42.44^{+2.22}_{-2.08}$
R_p (R_{\oplus})	$3.89^{+0.19}_{-0.20}$
a (AU)	$0.262^{+0.002}_{-0.002}$
ρ_p (g cm^{-3})	$3.98^{+0.62}_{-0.64}$
T_{eq}^1 (K)	385^{+17}_{-17}
$\langle F \rangle$ ($\times 10^7 \text{ erg s}^{-1} \text{ cm}^{-2}$)	1.01 ± 0.03
Instrumental parameters	
M_{TESS} (ppm)	$-0.000\ 0027^{+0.000\ 0028}_{-0.000\ 0027}$
$\sigma_{w,\text{TESS}}$ (ppm)	$1.836^{+12.323}_{-1.570}$
$q1_{\text{TESS}}$	$0.389^{+0.109}_{-0.073}$
$q2_{\text{TESS}}$	$0.848^{+0.108}_{-0.183}$
μ_{PFS1} (m s^{-1})	$0.77^{+0.36}_{-0.35}$
$\sigma_{w,\text{PFS1}}$ (m s^{-1})	$2.31^{+0.32}_{-0.28}$
μ_{HARPS} (m s^{-1})	$3.83^{+0.59}_{-0.56}$
$\sigma_{w,\text{HARPS}}$ (m s^{-1})	$1.61^{+0.54}_{-0.40}$
μ_{PFS2} (m s^{-1})	$-1.01^{+0.27}_{-0.28}$
$\sigma_{w,\text{PFS2}}$ (m s^{-1})	$1.30^{+0.30}_{-0.26}$

Note. Estimated using a Bond albedo of 0.5.

Eylen et al. 2016). It could be that these highly metallic and massive planets were formed through collisions with other worlds after the protoplanetary disc had dispersed, stripping the planet of gas whilst enriching it with further metals. Indeed, the results here imply that the heavy element enrichment for HD 95338 b is of the order of $\sim 38 M_{\oplus}$. It is important to note that the radius measurement of this planet is sufficiently precise that modelling uncertainties are larger than statistical uncertainties. These principally include uncertainties in the EOS, the interior structure of the planet (core-dominated versus well mixed), and the rock-to-ice ratio of the metals. However, these

uncertainties do not endanger the qualitative conclusion that the planet is extremely metal-rich, and changes would often lead to an even higher inferred Z .

10 CONCLUSIONS

We present the discovery of a dense Neptune planet, which is currently the longest period planet known to transit a star brighter than $V = 9$. Moreover it is the first single transit confirmed planet from the *TESS* mission. It orbits the early-K star, HD 95338, and was originally detected using long-term RV measurements carried out as part of the Magellan/PFS Exoplanet Survey. Additional RV data from HARPS help to further constrain the period and orbital parameters of the candidate. *TESS* photometry shows a single transit observed in Sector 10. From our orbital parameters, we estimated the transit time, $T_c = 2458\ 585.929 \pm 0.84$, and found it to be consistent within the errors with the observed transit by *TESS*, $T_{c,\text{TESS}} = 2458\ 585.279$, strongly suggesting both signals originate from the same source, and adding credibility to the reality of the planetary nature of the object. After performing a joint model fit combining the radial velocities and the photometric measurements, we find the planet has a radius of $R_p = 3.89^{+0.19}_{-0.20} R_{\oplus}$ and a mass of $M_p = 42.44^{+2.22}_{-2.08} M_{\oplus}$, giving rise to an anomalously high density for this planet of $\rho_p = 3.98^{+0.62}_{-0.64} \text{ g cm}^{-3}$. Planet structure models place HD 95338 b as being consistent with an ice world based on its mass and radius. From our Bayesian retrieval framework, we estimated the heavy element content to be $Z = 0.90 \pm 0.03$, which translates into $\sim 38 M_{\oplus}$. Such a high metallic value requires additional modeling efforts to explain and therefore follow-up observations are crucial to arrive at a better understanding of the properties of the planet and also to further constrain models for how such a world could form in the first place. Moreover, the study of the spin-orbit alignment of the planet with respect to the star via Rossiter-McLaughlin observations could provide some insights on the past history of the system, such as interaction with companions and migration.

ACKNOWLEDGEMENTS

This paper includes data gathered with the 6.5-m Magellan Telescopes located at Las Campanas Observatory, Chile. Additional observations were acquired with the ESO 3.6-m telescope at La Silla Observatory under programs 0101.C-0497, 0102.C-0525, and 0103.C-0442. We thank N. Espinoza for useful discussion during the preparation of this paper. MRD acknowledges the support by Comision Nacional de Investigacion Cientifica y Tecnologica (CONICYT)-PFCHA/Doctorado Nacional-21140646, Chile. JSJ acknowledges the support by Fondo Nacional de Desarrollo Cientifico y Tecnologico (FONDECYT) grant 1161218 and partial support by Centro Astrofisica y Tecnologias Afines (CATA)-Basal (PB06, CONICYT). JV acknowledges the support by CONICYT-PFCHA/Doctorado Nacional-21191829. DD acknowledges the support by NASA through Caltech/JPL grant RSA-1006130 and through the *TESS* Guest Investigator Program Grant 80NSSC19K1727. ZMB acknowledges funds from CONICYT/FONDECYT postdoctorado 3180405. This paper includes data collected by the *TESS* mission. Funding for the *TESS* mission is provided by the NASA Explorer Program.

DATA AVAILABILITY

The data underlying this study are available in this paper and in its online supplementary material.

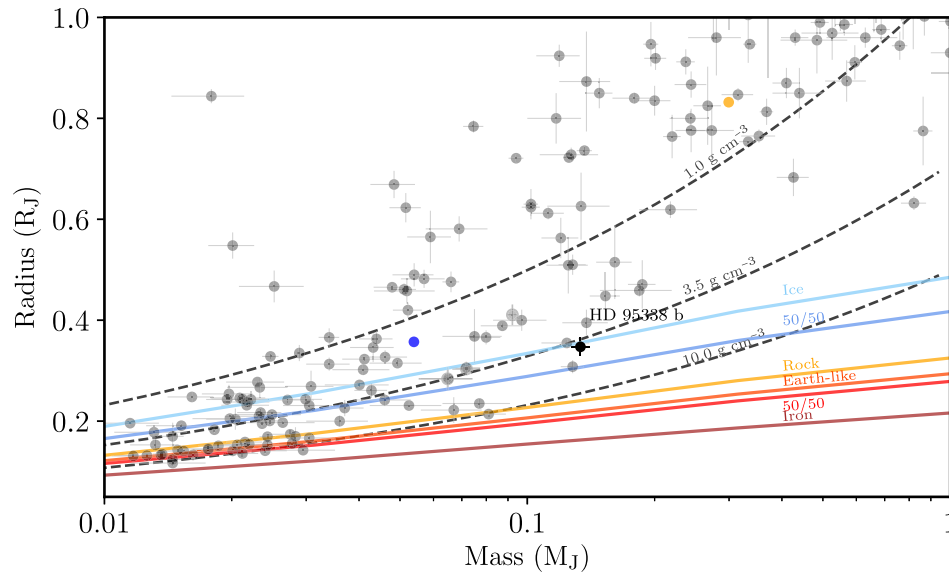


Figure 10. Mass–radius diagram. Grey circles represent confirmed exoplanets from TEPcat (Southworth 2011), which have radius measurements with a precision of 20 per cent or better. Neptune (blue) and Saturn (yellow) are included for comparison. Three iso-density curves are represented by the grey dashed lines. Composition models are from Fortney et al. (2007), and are shown by the coloured and labelled curves. The observed and derived parameters of HD 95388 b place this planet being consistent with an ice world (see the text).

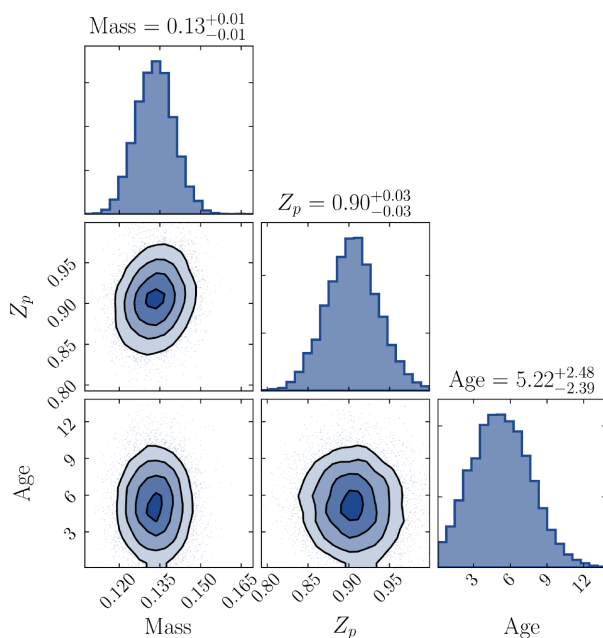


Figure 11. Corner plot showing the posteriors of heavy element content derived from the Bayesian retrieval framework described in Thorngren & Fortney (2019).

REFERENCES

- Allard F., Homeier D., Freytag B., 2012, *Phil. Trans. R. Soc. A*, 370, 2765
- Alonso-Floriano F. J. et al., 2019, *A&A*, 621, A74
- Anderson E., Francis C., 2012, *Astron. Lett.*, 38, 331
- Anglada-Escudé G., Butler R. P., 2012, *ApJS*, 200, 15
- Baglin A. et al., 2006, 36th COSPAR Scientific Assembly. p. 3749
- Bakos G. Á. et al., 2013, *PASP*, 125, 154
- Baliunas S., Sokoloff D., Soon W., 1996, *ApJ*, 457, L99
- Batalha N. M. et al., 2011, *ApJ*, 729, 27
- Birkby J. L., de Kok R. J., Brogi M., de Mooij E. J. W., Schwarz H., Albrecht S., Snellen I. A. G., 2013, *MNRAS*, 436, L35
- Boisse I., Bouchy F., Hébrard G., Bonfils X., Santos N., Vauclair S., 2011, *A&A*, 528, A4
- Borucki W. J. et al., 2010, *Science*, 327, 977
- Bouchy F. et al., 2005, *A&A*, 444, L15
- Bourrier V. et al., 2013, *A&A*, 551, A63
- Brahm R. et al., 2016, *AJ*, 151, 89
- Brahm R. et al., 2019, *AJ*, 158, 45
- Brogi M., Giacobbe P., Guilluy G., de Kok R. J., Sozzetti A., Mancini L., Bonomo A. S., 2018, *A&A*, 615, A16
- Butler R. P., Marcy G. W., Williams E., McCarthy C., Dossanah P., Vogt S. S., 1996, *PASP*, 108, 500
- Casasayas-Barris N. et al., 2019, *A&A*, 628, A9
- Castelli F., Kurucz R. L., 2004, preprint ([arXiv:astro-ph/0405087](https://arxiv.org/abs/astro-ph/0405087))
- Chabrier G., Mazevet S., Soubiran F., 2019, *ApJ*, 872, 51
- Charbonneau D., Brown T. M., Latham D. W., Mayor M., 2000, *ApJ*, 529, L45
- Charbonneau D., Brown T. M., Noyes R. W., Gilliland R. L., 2002, *ApJ*, 568, 377
- Crane J. D., Shtetman S. A., Butler R. P., 2006, in McLean I. S., Iye M., eds, Proc. SPIE Conf. Ser. Vol. 6269, Ground-based and Airborne Instrumentation for Astronomy. SPIE, Bellingham, p. 626931
- Crane J. D., Shtetman S. A., Butler R. P., Thompson I. B., Burley G. S., 2008, in McLean I. S., Casali M. M., eds, Proc. SPIE Conf. Ser. Vol. 7014, Ground-based and Airborne Instrumentation for Astronomy II. SPIE, Bellingham, p. 701479
- Crane J. D., Shtetman S. A., Butler R. P., Thompson I. B., Birk C., Jones P., Burley G. S., 2010, in McLean I. S., Ramsay S. K., Takami H., eds, Proc. SPIE Conf. Ser. Vol. 7735, Ground-based and Airborne Instrumentation for Astronomy III. SPIE, Bellingham, p. 773553
- Díaz M. R. et al., 2018, *AJ*, 155, 126
- Díaz M. R. et al., 2020, *MNRAS*, 493, 973
- Dotter A., 2016, *ApJS*, 222, 8
- Dragomir D. et al., 2019, *ApJ*, 875, L7
- Espinoza N., 2018, *Res. Notes AAS*, 2, 109
- Espinoza N., Kossakowski D., Brahm R., 2019, *MNRAS*, 490, 2262

- Feng F., Tuomi M., Jones H. R. A., Butler R. P., Vogt S., 2016, *MNRAS*, 461, 2440
- Feng F., Tuomi M., Jones H. R. A., 2017, *MNRAS*, 470, 4794
- Feng F. et al., 2019a, *ApJS*, 242, 25
- Feng F., Anglada-Escudé G., Tuomi M., Jones H. R. A., Chanamé J., Butler P. R., Janson M., 2019b, *MNRAS*, 490, 5002
- Fortney J. J., Marley M. S., Barnes J. W., 2007, *ApJ*, 659, 1661
- Fulton B. J., Petigura E. A., Blunt S., Sinukoff E., 2018, *PASP*, 130, 044504
- Gaia Collaboration et al., 2018, *A&A*, 616, A1
- Haario H., Saksman E., Tamminen J., 2001, *Bernoulli*, 7, 223
- Haario H., Laine M., Mira A., Saksman E., 2006, *Stat. Comput.*, 16, 339
- Hauschildt P. H., Allard F., Baron E., 1999, *ApJ*, 629, 865
- Henry G. W., Marcy G. W., Butler R. P., Vogt S. S., 2000, *ApJ*, 529, L41
- Hidalgo D. et al., 2020, *A&A*, 636, 13
- Howell S. B. et al., 2014, *PASP*, 126, 398
- Husser T.-O., von Berg S. W., Dreizler S., Homeier D., Reiners A., Barman T., Hauschildt P. H., 2013, *A&A*, 553, A6
- Jenkins J. S., Tuomi M., 2014, *ApJ*, 794, 110
- Jenkins J. S. et al., 2017, *MNRAS*, 466, 443
- Jenkins J. S. et al., 2020, *Nature*, in press
- Jordán A. et al., 2019, *AJ*, 159, 145
- Kass R. E., Raftery A. E., 1995, *J. Am. Stat. Assoc.*, 90, 773
- Kipping D. M., 2013, *MNRAS*, 435, 2152
- Kostov V. B. et al., 2014, *ApJ*, 784, 14
- Kreidberg L., 2015, *PASP*, 127, 1161
- Kreidberg L. et al., 2015, *ApJ*, 814, 66
- Kurucz R. L., 1993, *VizieR Online Data Catalog VI/39*, 6039
- Lecavelier des Etangs A. et al., 2012, *A&A*, 543, L4
- Léger A. et al., 2009, *A&A*, 506, 287
- Levenberg K., 1944, *Q. Appl. Math.*, 2, 164
- Lomb N. R., 1976, *Ap&SS*, 39, 447
- Lovis C. et al., 2011, preprint ([arXiv:1107.5325](https://arxiv.org/abs/1107.5325))
- Marquardt D. W., 1963, *J. Soc. Ind. Appl. Math.*, 11, 431
- Mayo A. W. et al., 2019, *AJ*, 158, 165
- Metropolis N., Rosenbluth A. W., Rosenbluth M. N., Teller A. H., Teller E., 1953, *J. Chem. Phys.*, 21, 1087
- Morton T. D., 2015, *Astrophysics Source Code Library*, record ascl:1503.010
- Mulders G. D., Pascucci I., Apai D., Ciesla F. J., 2018, *AJ*, 156, 24
- Nascimbeni V., Piotto G., Pagano I., Scandariato G., Sani E., Fumana M., 2013, *A&A*, 559, A32
- Pepe F. et al., 2002, *The Messenger*, 110, 9
- Pojmanski G., 1997, *Acta Astron.*, 47, 467
- Ricker G. R. et al., 2015, *J. Astron. Telesc. Instrum. Syst.*, 1, 014003
- Salz M., Czesla S., Schneider P. C., Schmitt J. H. M. M., 2016, *A&A*, 586, A75
- Sandford E., Espinoza N., Brahm R., Jordán A., 2019, *MNRAS*, 489, 3149
- Scargle J. D., 1982, *ApJ*, 263, 835 (GLS)
- Schlafly E. F., Finkbeiner D. P., 2011, *ApJ*, 737, 103
- Schlegel D. J., Finkbeiner D. P., Davis M., 1998, *ApJ*, 500, 525
- Skrutskie M. F. et al., 2006, *AJ*, 131, 1163
- Snedden C. A., 1973, PhD thesis, The University of Texas at Austin
- Soto M. G., Jenkins J. S., 2018, *A&A*, 615, A76
- Southworth J., 2011, *MNRAS*, 417, 2166
- Speagle J. S., 2019, *MNRAS*, 493, 3132
- Thompson S. L., 1990, *ANEOS Analytic Equations of State for Shock Physics Codes Input Manual*. Sandia National Laboratories, Albuquerque, New Mexico
- Thorngren D., Fortney J. J., 2019, *ApJ*, 874, L31
- Thorngren D. P., Fortney J. J., Murray-Clay R. A., Lopez E. D., 2016, *ApJ*, 831, 64
- Tuomi M., Jones H. R. A., Barnes J. R., Anglada-Escudé G., Jenkins J. S., 2014, *MNRAS*, 441, 1545
- Turner J. D. et al., 2020, *ApJ*, 888, L13
- Van Eylen V. et al., 2016, *AJ*, 152, 143
- Wheatley P. J. et al., 2017, *MNRAS*, 475, 4476
- Wytttenbach A., Ehrenreich D., Lovis C., Udry S., Pepe F., 2015, *A&A*, 577, A62
- Zechmeister M., Kürster M., 2009, *A&A*, 496, 577
- Zinn J. C., Pinsonneault M. H., Huber D., Stello D., 2019, *ApJ*, 878, 136

SUPPORTING INFORMATION

Supplementary data are available at [MNRAS](https://www.mnras.org) online.

pfs1.txt
pfs2.txt
terra.txt

Please note: Oxford University Press is not responsible for the content or functionality of any supporting materials supplied by the authors. Any queries (other than missing material) should be directed to the corresponding author for the article.

This paper has been typeset from a \TeX/L\AA\TeX file prepared by the author.